International Journal of Innovative
Computing, Information and Control
Volume **9**, Number **6**, June **2013**

 ISSN 1349-4198
pp. 2421–2440

A CLOUD REMOVAL APPROACH FOR AERIAL IMAGE VISUALIZATION

Din-Chang Tseng* and Chun-Liang Chien

Institute of Computer Science and Information Engineering
National Central University
No. 300, Jungda Rd., Chungli 32001, Taiwan
*Corresponding author: tsengdc@ip.csie.ncu.edu.tw; jameschyan@csie.ncu.edu.tw

Received March 2012; revised July 2012

Abstract. *Partial cloud cover is a serious problem in synthesis of virtual scene and terrain models. The problem can be mostly resolved by mosaicking the cloud areas with the cloud-free areas in other temporal images. In this study, a complete approach, including image enhancement, cloud detection, cloud areas mosaicking, and image feathering, is proposed to generate cloud-free images from multi-temporal satellite images. At first, all original images were enhanced by the intensity histogram equalization in the proposed exact HSI (eHSI) color space, and the gamut problem could be avoided. Second, a simple intensity thresholding method was used to extract all cloud pixels, and then a difference checking was used to release the fixed-flat-white land covers in the eHSI color space. Third, all images were divided into grid zones, and then the cloud zones in the base image were replaced with same-location, cloud-free zones from other temporal images. Finally, a color uniformity method and a pyramid multiscale feathering method were used to feather the replaced cloud zones to generate realistic, cloud-free satellite images. Based on the proposed complete approach, not only were the clouds removed in the resulting images, but also, the resulting images show proper brightness and saturation. Moreover, the effect of the proposed methods is demonstrated and compared with other existing methods.*
Keywords: Image synthesis, Cloud removal, Image enhancement, Image fusion, Multi-temporal aerial images

1. **Introduction.** In recent decades, a tremendous number of remote sensing images have been received and widely used for many applications, such as geographical visualization, terrain visualization, scene analysis, land-use classification, landscape ecological change detection. Regardless of the purpose for which the Earth resource satellite images are used, the first step is to extract landscape information from the images. However, the images acquired from satellites may be interfered by clouds and cloud shadows in certain weather conditions, especially in humid tropical areas. Generally, cloud cover does not always appear in the same location; therefore, if multi-temporal images are acquired at different times over a specific region, the complement of multi-temporal images acquired might solve the cloud cover problem. In other words, the cloud-free images may be generated by replacing the cloud areas with cloud-free areas from other multi-temporal images.

The generation of cloud-free satellite images is a traditional topic. The complete steps for producing cloud-free images generally include cloud determination and image fusion. Three different types of cloud removal approaches have been proposed: (*i*) treating cloud as noise and removing it, (*ii*) using "multispectral" images to fuse and generate cloud-free images, and (*iii*) using "multitemporal" images to fuse and generate cloud-free images. The first type of method [1] generally uses spectral information to filter out the cloud

pixels. Arellano [2] applied wavelet transform to detect clouds and cloud shadows, and then filled in the missing information with multi-temporal *ASTER* images. Wang *et al.* [3] proposed an automated cloud detection method by simply thresholding the high-frequency components in the discrete wavelet transform of two fusing images. Kubo *et al.* [4] represented the cloud distribution as texture, and then used Gabor wavelet transform to detect local regularity to extract cloud regions. Li *et al.* [5] used non-separable wavelet frame transform (*NWFT*) to fuse two registered images: one is a high spatial-resolution panchromatic image, and the other is a low spatial-resolution multispectral image. This type of method is simple, but bright and large land-cover areas have similar spectral characteristics as clouds, and they also might be filtered out; moreover, denoising methods cannot completely recover the land covers blocked by the clouds.

The second type of method [6, 7, 8] only uses multispectral images to detect and remove clouds. Generally, the clouds appear in almost all bands of multispectral images; thus, the clouds can only be treated as noise, and results similar to the first type of method are obtained.

The third type of method [2, 3, 9, 10, 11, 12, 13] is the mainstream; most researchers used both multispectral and multi-temporal data, accompanied by various algorithms, to generate cloud-free images. These methods use the *NDVI* test [2], reflectance difference checking with other regions [3], regression tree modeling with histogram matching [10], band-ratio classification with size/shape checking [11], pixel ranking [12], or intensity thresholding [13] to decide whether a region is covered by cloud or not. Gabarda and Cristóbal [9] used a one-dimensional pseudo-Wigner distribution (*PWD*) transformation and a pixel-wise cloud model to fuse two partial-cloudy images to generate a cloud-free image. These methods can achieve good results under some special conditions; however, most are too simple to detect the cloud regions accurately.

Most related studies did not consider the problem of image enhancement to make the resulting images have less visual difference, such as the images for Google map, Google Earth, Nokia Maps 3D. In this study, a complete multi-temporal approach including image enhancement, cloud detection, image mosaicking, and image feathering, is proposed in order to produce cloud-free images. At first, all original *RGB* images were transformed to the proposed exact *HSI* (*eHSI*) color space [14]; their intensity components were then equalized, and the gamut problem was avoided. The purpose of this study was to improve aerial geometrical visualization, such as Google Earth; thus, the original *RGB* aerial images were used. Second, a simple intensity thresholding technique was used to extract all cloud pixels. The fixed-white land surfaces may be extracted as well; thus, a *difference checking* method was used to release them by comparing the difference between two temporal images, and a morphological *opening* operation was accomplished to exclude the small noise. Third, all source images were divided into grid zones, and then *cloud zones* in the *base image* were replaced with the corresponding zone in the replacing images, where the base image is one of the source images that has least thin-cloud cover, and the others are the replacing images. Finally, a color uniformity method and a pyramid multiscale feathering method [15] were used to generate cloud-free images with proper brightness and saturation.

The remaining sections of this paper are organized as follows. Section 2 describes the intensity enhancement method in the proposed *eHSI* color space. Section 3 presents the proposed method for determining cloud and cloud-shadow zones in the base image. Section 4 presents the pyramid multi-scale fusion method to make seams invisible in the fused images. Section 5 reports the experiments of the proposed methods on image enhancement, cloud determination, and image fusion. Finally, conclusions are given in Section 6.

2. **Multi-spectral Image Enhancement.** Pseudo *SPOT* images were processed in this study. The original *SPOT* images we obtained were generally dark and had low contrast; thus, their intensity component should be enhanced. The enhancement process not only improved the visual quality of the final results, but also simplified the cloud detection procedure.

2.1. **Conventional problems in color image enhancement.** Histogram equalization is a well-known image contrast enhancement method and has been used for various image enhancements [16, 17, 18, 19]. However, it often produces images with unnatural appearances and visually disturbing artifacts. One reason for the unwanted effects is that the histogram equalization attempts to force the output image to have a uniform gray-level distribution, regardless of what the original gray-level distribution is. A better solution should consider the original gray-level distribution to ensure that the output image not only has enhanced visibility and contrast, but also is faithful to the original appearance. Hence, for color image enhancement, the original *RGB* image is usually transformed into a perceptual color space, and the intensity and/or saturation components are enhanced, but they keep the hue component unaltered to preserve the hue of the original image.

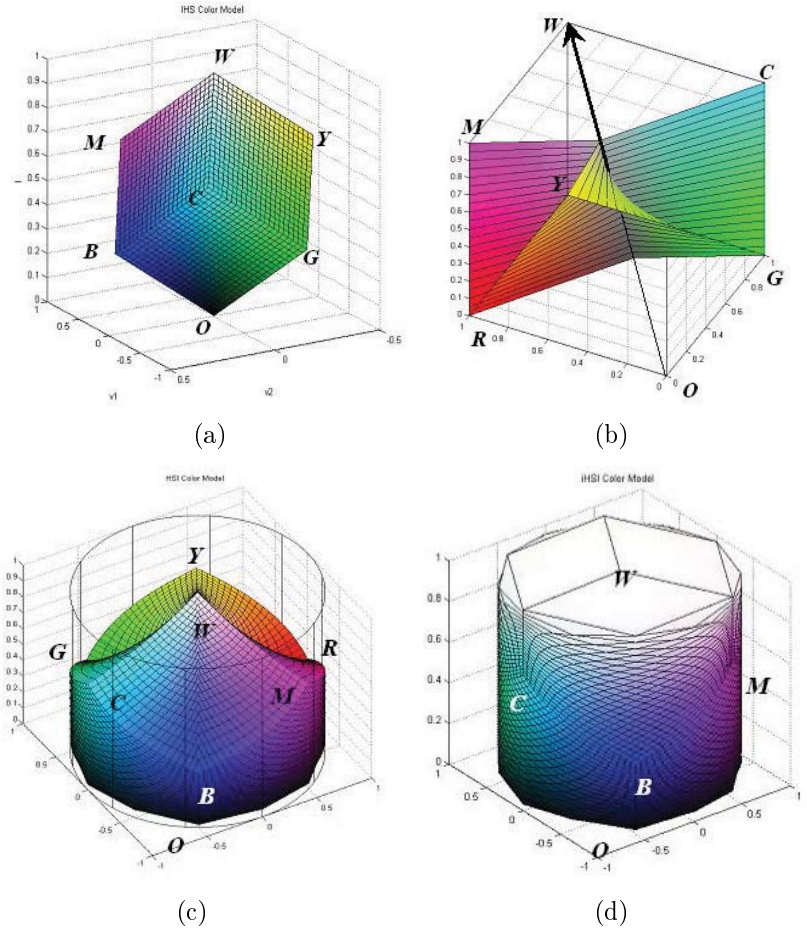

FIGURE 1. The saturation conversion is improved to resolve the out of gamut problem. (a) The RGB color cube. (b) The boundary for determining the usage of the traditional saturation formula or the proposed saturation formula. (c) The traditional HSI color model. (d) The proposed eHSI color model.

Weeks *et al.* [20] mentioned that the enhancement procedure usually experiences the gamut problem. Therefore, they proposed a hue-preserving color image enhancement technique that modifies the intensity and saturation components in the color difference (C-Y) color space. The equalization process begins by segmenting the C-Y color space into N hue regions and K luminance regions. The method has no specific criterion to decide which component should be enhanced first; furthermore, the method has no specific criterion to decide the subspace numbers, N and K.

2.2. **Conventional problems in the *HSI* color space.** The conventional *HSI* color space [21] is derived by normalizing the three lower-intensity planes (*ORYG*, *OGCB*, and *OBMR* planes) of the *RGB* cube, shown in Figure 1(a), to a circular shape, as shown in the lower portion of Figure 1(c). The upper portion of the *HSI* color model is "collapsed", so that the pixels can go out of the gamut if their intensity values are substituted with a higher value. If the pixels go out of the gamut, their intensity and saturation values will be clipped after they are transformed back to the *RGB* color space [14]. As illustrated in Figure 2(a), if the intensity value of pixel a is substituted from I_1 to I_2, it will be shifted to position b' rather than b, because it goes out of the gamut. Hence, its intensity and saturation components are both enhanced and clipped. As an example, shown in Figure 2(c), after intensity histogram equalization, the cloud areas cannot be enhanced to pure

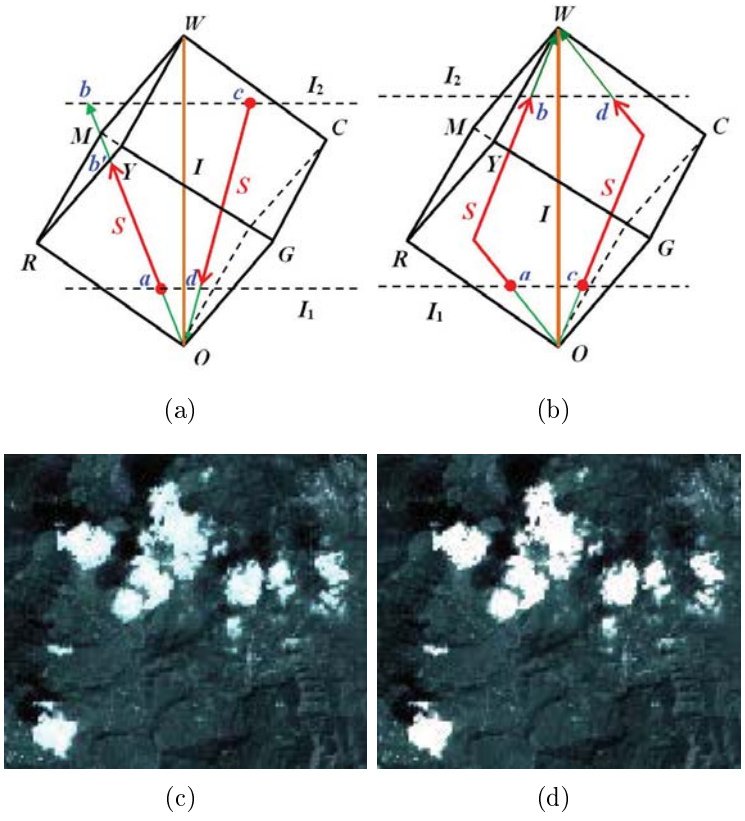

FIGURE 2. The saturation variation coincides with the intensity adjustment. (a) Intensity adjustment in the traditional HSI color model. (b) Intensity adjustment in the proposed eHSI color model. (c) The image was enhanced based on the traditional HSI color model; the cloud is not pure white. (d) The image was enhanced based on the proposed eHSI color model; the cloud is pure white.

white, because of the gamut problem and clipping operation. As such, it is difficult to separate the cloud pixels from other land cover pixels by a simple thresholding method. On the other hand, if the intensity of pixel c is substituted from I_2 to I_1, it will be shifted from c to d, as shown in Figure 2(a), and not only the intensity component, but also the saturation component, is reduced. To avoid the gamut problem, the HSI color space is improved, and the clipping operation will no longer be required.

2.3. **Review of the proposed eHSI color space.** As described in [14], the *RGB* cube is separated into two symmetrical parts by a boundary, as shown in Figure 1(b). If the intensity value of a pixel is lower than the boundary, the pixel will be transformed by using the conventional *RGB* to *HSI* transformation; otherwise, it will be transformed by the *RGB* to *eHSI* transformation, which is derived by normalizing the three higher-intensity planes (*WYGC*, *WCBM*, and *WMRY*) to a circular shape, as shown in Figure 1(d). The complete *RGB* to *eHSI* transformation is defined as follows [14]:

if $I > \dfrac{2}{3} - \dfrac{|H \mod 120^\circ - 60^\circ|}{180^\circ}$

$$S = 1 - \frac{3(1 - \max(R, G, B))}{3 - (R + G + B)}, \tag{1}$$

otherwise,

$$S = 1 - \frac{3\min(R, G, B)}{R + G + B}. \tag{2}$$

After the transformation, the saturation range of the *eHSI* color space is normalized in the range of [0, 1]; hence, the intensity component of a pixel can be freely manipulated in the [0, 1] range without generating the gamut problem.

After pixels are processed in the *eHSI* color space, they will be transformed back to the *RGB* color space for display. The complete *eHSI* to *RGB* transformation is defined as follows:

RG section: $0 < H \le 120^\circ$ & $I \le \dfrac{2}{3} - \dfrac{|H - 60^\circ|}{180^\circ}$

$$\begin{cases} B = I(1 - S) \\ R = I\left[1 + \dfrac{S\cos(H)}{\cos(60^\circ - H)}\right] \\ G = 3I - (R + B) \end{cases} \tag{3}$$

GB section: $120^\circ < H \le 240^\circ$ & $I \le \dfrac{2}{3} - \dfrac{|H - 180^\circ|}{180^\circ}$

$$H = H - 120^\circ$$
$$\begin{cases} R = I(1 - S) \\ G = I\left[1 + \dfrac{S\cos(H)}{\cos(60^\circ - H)}\right] \\ B = 3I - (R + G) \end{cases} \tag{4}$$

BR section: $240^\circ < H \le 360^\circ$ & $I \le \dfrac{2}{3} - \dfrac{|H - 300^\circ|}{180^\circ}$

$$H = H - 240^\circ$$
$$\begin{cases} G = I(1 - S) \\ B = I\left[1 + \dfrac{S\cos(H)}{\cos(60^\circ - H)}\right] \\ R = 3I - (G + B) \end{cases} \tag{5}$$

YC section: $60^\circ < H \leq 180^\circ$ & $I > \dfrac{1}{3} + \dfrac{|H - 120^\circ|}{180^\circ}$

$$H = H - 240^\circ$$
$$\begin{cases} G = I(1-S) + S \\ B = 1 - (1-I)\left[1 + \dfrac{S\cos(H)}{\cos(60^\circ - H)}\right] \\ R = 3I - (G+B) \end{cases} \tag{6}$$

CM section: $180^\circ < H \leq 300^\circ$ & $I > \dfrac{1}{3} + \dfrac{|H - 240^\circ|}{180^\circ}$

$$\begin{cases} B = I(1-S) + S \\ R = 1 - (1-I)\left[1 + \dfrac{S\cos(H)}{\cos(60^\circ - H)}\right] \\ G = 3I - (R+B) \end{cases} \tag{7}$$

MY section: $\left(300^\circ < H \leq 360^\circ \;\&\; I > \dfrac{1}{3} + \dfrac{H - 60^\circ}{180^\circ}\right)$
or $\left(0^\circ < H \leq 60^\circ \;\&\; I > \dfrac{1}{3} + \dfrac{H}{180^\circ}\right)$

$$H = H - 120^\circ$$
$$\begin{cases} R = I(1-S) + S \\ G = 1 - (1-I)\left[1 + \dfrac{S\cos(H)}{\cos(60^\circ - H)}\right] \\ B = 3I - (R+G) \end{cases} \tag{8}$$

As illustrated in Figure 2(b), if the intensity component of a pixel is substituted from I_1 to I_2 in the *eHSI* color space, it will be shifted from position a to b or c to d, respectively. It is noted that the saturation component is linearly adapted according to the maximum attainable saturation range, and the intensity substitutions are all achievable without the gamut problem. Therefore, after intensity equalization in the *eHSI* color space, the cloud areas can be enhanced to pure white, as shown in Figure 2(d), and then, a simple thresholding method can be used to separate the cloud pixels from other land cover pixels. The proposed image enhancement algorithm is described as follows.

Algorithm 2.1. *Color image enhancement based on the eHSI color space.*

Step 1: *Transform the original color image I from the RGB color space into the eHSI color space.*

Step 2: *Equalize the intensity component of image I using* [21]

$$s_k = T(r_k) = \sum_{j=0}^{k} \frac{n_j}{n}, \quad k = 0, 1, 2, \ldots, L-1, \tag{9}$$

where n is the total number of pixels in the image, n_k is the number of pixels that have gray level r_k, $[0, L-1]$ is the gray scale, and s_k is the transformed gray level.

Step 3: *Transform the equalized image from the eHSI color space back to the RGB color space.*

With the proposed intensity enhancement algorithm, the intensity and saturation components of the images shown in Figures 3(a) and 3(b) were enhanced, and the color is undistorted, as shown in Figures 3(c) and 3(d). Furthermore, the cloud pixels are enhanced to pure white, so that they can be separated easily from most land cover pixels.

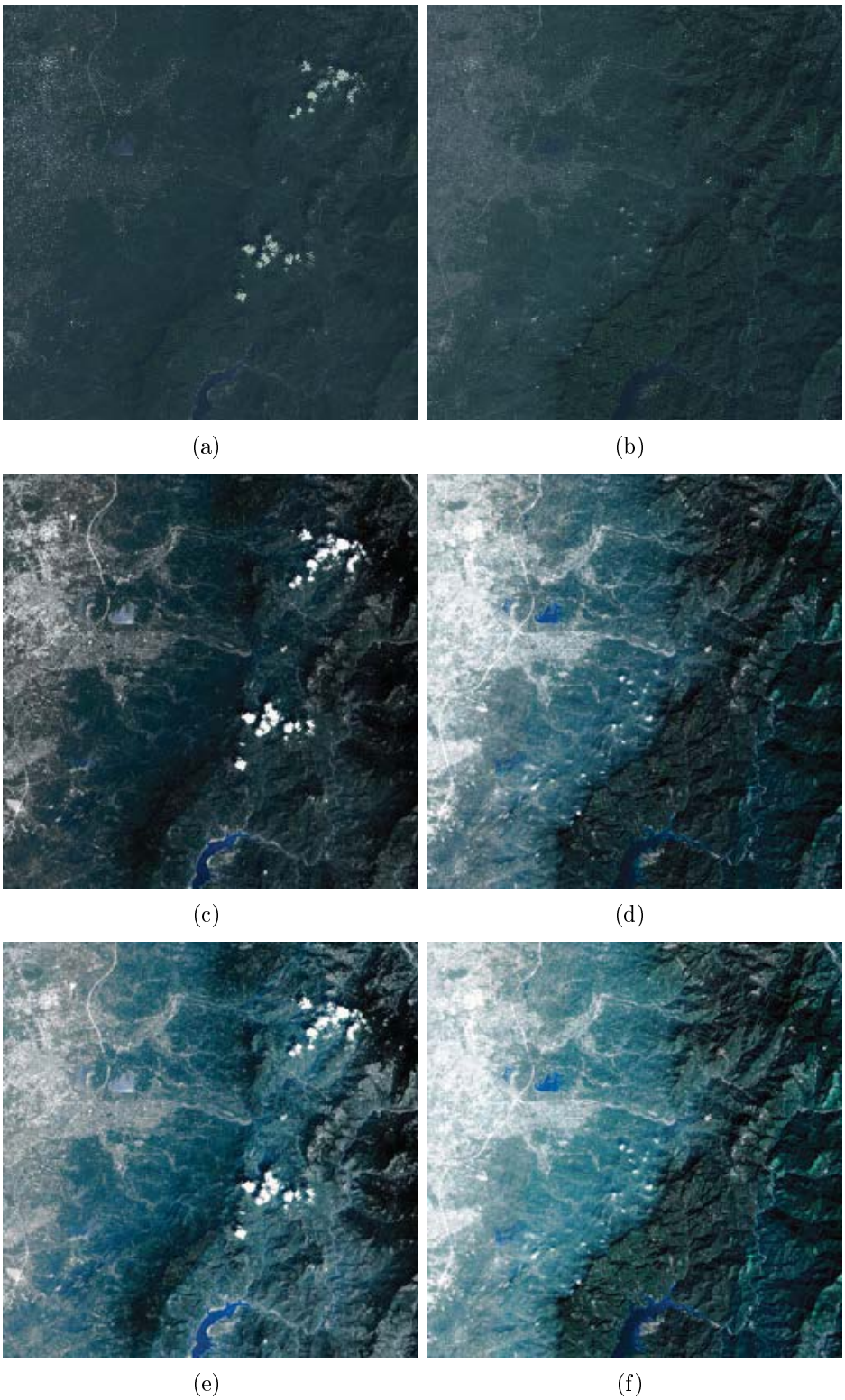

(a) (b)

(c) (d)

(e) (f)

FIGURE 3. The image enhancement results. (a) and (b) The original images. (c) and (d) The intensity histogram of the original images is linearly stretched. (e) and (f) The intensity histogram is concentrated by an *S-type* function.

2.4. **Tradeoff between intensity and saturation component.** Weeks *et al.* [20] mentioned that there is a tradeoff between the intensity and saturation components of an image. In the *eHSI* color space, the saturation component of an image can be enhanced by sacrificing a little contrast, as described in [14]. We have stated that the saturation component is adaptively expanded according to the maximum attainable saturation range in the *eHSI* color space. Hence, the saturation component can be enhanced by centralizing the intensity component into the central intensity range, because there is a wider saturation range to expand. The complete approaches are described as follows.

Algorithm 2.2. *Saturation enhancement based on intensity centralization.*

Step 1: *Estimate the central moment of the intensity component by*

$$\overline{k} = \frac{\sum_k n_k k}{\sum_k n_k}, \quad k = 0, 1, 2, \ldots, L-1, \tag{10}$$

where n_k is the number of pixels that have gray level k, $[0, L-1]$ is the gray scale, and $\overline{k}$ is the central moment.

Step 2: *Deform the intensity histogram by shifting $\overline{k}$ to the center of intensity range C using*

$$\begin{cases} k' = \dfrac{kC}{\overline{k}}, & \text{if } k \le \overline{k} \\ k' = L - \dfrac{(L-k)C}{L-\overline{k}}, & \text{if } k > \overline{k} \end{cases} \tag{11}$$

Step 3: *Use the S-type function to centralize the intensity to the central region. The S-type function is defined as*

$$f(x) = \begin{cases} 0.5\left(\dfrac{x}{0.5}\right)^n, & 0 \le x \le 0.5 \\ 1 - 0.5\left(\dfrac{1-x}{0.5}\right)^n, & 0.5 < x \le 1 \end{cases} \tag{12}$$

where n is a constant. For example, if $n = 0.5$, Equation (12) can be expressed as

$$f(x) = \begin{cases} \sqrt{0.5x}, & 0 \le x \le 0.5 \\ 1 - \sqrt{0.5(1-x)}, & 0.5 < x \le 1 \end{cases} \tag{13}$$

With the proposed saturation enhancement algorithm, two more saturated images were obtained, as shown in Figures 3(e) and 3(f). The saturation component is linearly expanded so that the oversaturated achromatic region mentioned in [20] does not appear in these results.

3. **Cloud Detection.** The determination of cloud and cloud-shadow regions is one of the key tasks for cloud removal. This study considered three assumptions: (*i*) the cloud regions are smooth and flat, (*ii*) the color of the clouds is white, and (*iii*) clouds rarely appear in the same position in different temporal images.

Based on assumption (*i*), a spatial-frequency analysis technique and a proposed gradient analysis technique were used to detect the smooth and flat regions; this will be described in Sections 3.1 and 3.2, respectively. Based on assumption (*ii*), a color-based thresholding method was used to detect the white color regions; this will be described in Section 3.3. An additional difference checking, based on assumption (*iii*), was performed after the above three processes, in order to release the fixed-flat-white land covers that could not be distinguished from clouds by the previous two assumptions.

3.1. **Spatial-frequency analysis method.** The smoothness of a local region can be evaluated by spatial-frequency analysis. Several formulas have been proposed to evaluate the spatial-frequency relationship including the short-term Fourier transform ($STFT$) [22], wavelet transform [23], and Wigner distribution (WD) [24]. Gabarda and Cristóbal [9] used the pseudo-Wigner distribution (PWD) method to evaluate the local spatial frequency of cloudy images. The PWD method is pixel-based replacement rather than region-based replacement; the PWD method always selects the lowest-distance pixel from one of the different temporal images as the resulted pixel. If the appearances of the different temporal images are similar, this method can get good results. However, if the image appearances are different, this method will randomly select pixels between two different temporal images to synthesize an intermixture result. Furthermore, this method cannot tell us whether a pixel is in a cloud area or not.

To solve this problem, the PWD distance of a pixel is thresholded, so that a pixel will be classified as a cloud pixel if its PWD distance is lower than a pre-defined threshold value. The complete algorithm is described as follows.

Algorithm 3.1. *Cloud detection using spatial-frequency analysis technique.*

Step 1: *Transform two original color images into two gray-level images, I_a and I_b.*

Step 2: *Calculate the PWD of I_a and I_b, respectively, and the PWD of $I(x, y)$ is given by*

$$PWD(x, y) = W(X) = 2 \sum_{k=-N/2}^{N/2-1} I(x + k, y) I^*(x - k, y) \exp\left(\frac{-j2\pi kX}{N}\right) \tag{14}$$

where $*$ denotes complex conjugate.

Step 3: *Calculate the PWD distance between $PWD(x, y)$ and the PWD of cloud W_{cloud}, where W_{cloud} is defined in* [9] *as $[0, 0, \ldots, 1, \ldots, 0, 0]$, and the PWD distance $D(x, y)$ is defined as*

$$D(x, y) = \|PWD(x, y) - W_{cloud}\| \tag{15}$$

Step 4: *Threshold the pixels with low PWD distance in $D(x, y)$; the result is denoted as $T(x, y)$. The threshold value is defined as 0.1; thus, if $D(x, y) < 0.1$, then $T(x, y) = 1$; otherwise, $T(x, y) = 0$.*

One example of cloud detection Algorithm 3.1 is shown in Figure 4(a). It is noted that the reservoir and some urban land covers were also extracted. To resolve this problem, an additional difference checking between two source images was used to get rid of the fixed-flat land covers, based on assumption (*iii*). Moreover, a morphological *opening* operation was used to delete small regions. The complete algorithm is described as follows.

Algorithm 3.2. *Difference checking algorithm.*

Step 1: *Obtain the fixed land cover pixels $FD(x, y)$ by using the logical "And" operation, (i.e., $FD(x, y) = T_a(x, y) \wedge T_b(x, y)$).*

Step 2: *Remove the $FD(x, y)$ by subtracting $FD(x, y)$ from $T(x, y)$ (i.e., $T'(x, y) = T(x, y) - FD(x, y)$).*

Step 3: *Apply the morphological "Opening" operation on $T'(x, y)$ to get rid of small regions.*

By using the difference checking algorithm, the reservoir and most fixed land covers were successfully removed, as shown in Figure 4(b). The final results were superimposed on two source images, as shown in Figures 4(c) and 4(d). It can be observed that most cloud areas can be effectively detected, but the thin, broken clouds are not. On the

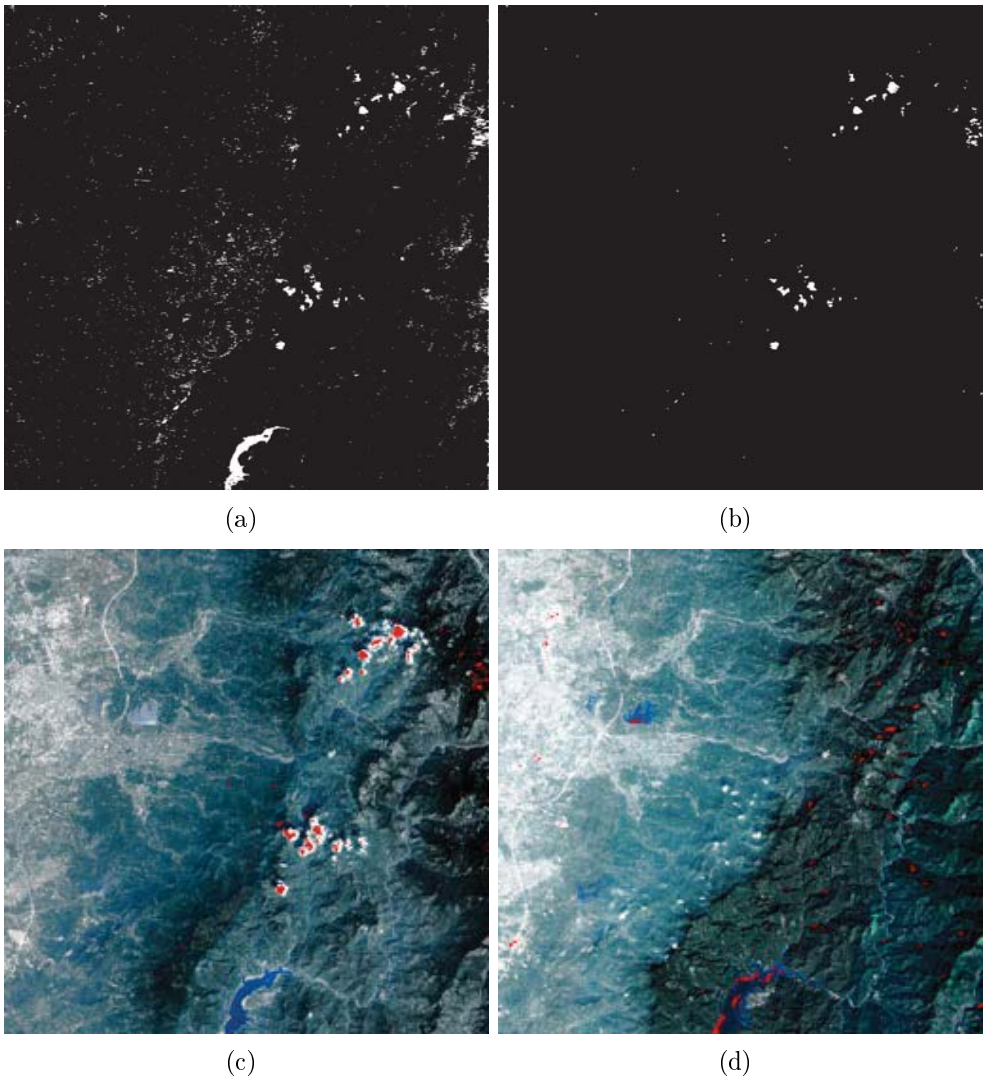

FIGURE 4. The frequency-based cloud detection. (a) The low spatial-frequency regions. (b) Excluding low difference area from (a) and then eliminating the small fragments. (c) Superimposing on the source image. (d) Another case.

other hand, Equation (14) is a row-major 1D Wigner distribution analysis, so the spatial-frequency analysis along the column direction is unavailable. If the small cloud areas are vertically aligned, their low frequency features will not be detected. Moreover, the *PWD* method has the "uncertainty principle" problem; that is, the sliding window size must be large enough to maintain the accuracy of frequency evaluation. However, if the window size is much larger than the cloud area, the actual cloud position cannot be detected; for example, the edges of cloud areas are eroded. Finally, some false alarms exist, especially in the dark valleys, because this method does not consider color information.

3.2. **Proposed gradient-based method.** The smoothness of a region can also be evaluated by the gradient [21], defined as $\nabla f = (\partial f/\partial x, \partial f/\partial y)$. Thus, a threshold value was used to classify whether or not a pixel had low gradient magnitude. Accordingly, an additional difference checking and a morphological Opening were used to eliminate the fixed-flat land covers and small regions. The complete algorithm is described as follows.

Algorithm 3.3. *Cloud detection using gradient analysis technique.*

Step 1: *Transform two original color images into two gray images, I_a and I_b.*

Step 2: *Calculate the gradient magnitude $G(x, y)$ of source image $I(x, y)$,*

$$G(x,y) = \sqrt{\left(\frac{\partial I(x,y)}{\partial x}\right)^2 + \left(\frac{\partial I(x,y)}{\partial y}\right)^2} \tag{16}$$

Step 3: *Threshold the pixels with low gradient magnitude in $G(x, y)$; the result is denoted as $T(x, y)$.*

Step 4: *Check difference using Algorithm 3.2.*

One example of cloud detection Algorithm 3.3 is shown in Figure 5(a) and most fixed land covers were successfully removed, as shown in Figure 5(b). The final results were superimposed on the original images, as shown in Figures 5(c) and 5(d). Most cloud areas can be effectively detected, and there are fewer false alarms than in the previous method, because the gradient magnitude evaluation is isotropic, rather than row-wise. However, small and broken cloud areas are still difficult to detect, and the boundaries of cloud areas are still eroded, because they have a high gradient. Furthermore, some false alarms still exist, because color information is not considered.

3.3. **Color-based method.** The pseudo SPOT images have a ground resolution of 6.25 meters; the information in a pixel may contain various materials, and the pixel is called a mixed pixel. The linear spectral unmixing (LSU) method [25] was generally used to solve the mixed pixel problem and generate a fraction image for each ground cover class based on a least-square-error criterion of a linear system [26]. For example, if the RGB value vector of pixel x in the source image is equal to (r, g, b), and n well-defined land cover classes is equal to $(r_1, g_1, b_1), \ldots, (r_n, g_n, b_n)$. Then, the pixel x can be represented by the combination of land cover classes as

$$\boldsymbol{x} = f_1 \begin{bmatrix} r_1 \\ g_1 \\ b_1 \end{bmatrix} + \ldots + f_N \begin{bmatrix} r_n \\ g_n \\ b_n \end{bmatrix} = \begin{bmatrix} r_1 & \ldots & r_n \\ g_1 & \ldots & g_n \\ b_1 & \ldots & b_n \end{bmatrix} \begin{bmatrix} f_1 \\ \vdots \\ f_n \end{bmatrix} = \begin{bmatrix} \boldsymbol{m}_1 \\ \vdots \\ \boldsymbol{m}_n \end{bmatrix}^{\mathrm{T}} \boldsymbol{f} = \boldsymbol{M}\boldsymbol{f} \tag{17}$$

where $\boldsymbol{m}_i$ is the i-th land cover class, $\boldsymbol{M}$ is composed of $\boldsymbol{m}_1, \ldots, \boldsymbol{m}_n$, and $\boldsymbol{f}$ is composed of the land cover class proportion of pixel $\boldsymbol{x}$. $\boldsymbol{f}$ can be estimated by using the least-squares method, as follows:

$$\boldsymbol{f} = (\boldsymbol{M}^{\mathrm{T}}\boldsymbol{M})^{-1}\boldsymbol{M}^{\mathrm{T}}\boldsymbol{x}. \tag{18}$$

To avoid non-unique solutions, the number of land cover classes n must be smaller or equal to the number of spectral bands. In this study, RGB color images are used, so that at most, three land cover classes can be defined. In practice, for the purpose of cloud detection, the proportion of different materials in a mixed pixel is insignificant; thus, the LSU method is no different from RGB thresholding. For example, to detect the white cloud pixels, m_1 can be defined as equal to (1, 1, 1) (white color), and m_2 and m_3 may be defined as two colors other than white; then, we check whether f_1 is greater than a threshold value. Another method is that m_1, m_2, and m_3 are defined as (1, 0, 0) (red), (0, 1, 0) (green), and (0, 0, 1) (blue), respectively, and then we check whether f_1, f_2, and f_3 are all greater than a threshold value. The second method is no different from the RGB component thresholding. To simplify the cloud detection procedure, the RGB thresholding method was used in this study.

As mentioned in Section 2.3, the cloud areas cannot be enhanced to pure white in the traditional HSI color space, so it is difficult to segment them by using a fixed intensity threshold, as shown in Figure 6(a). However, after intensity histogram equalization in

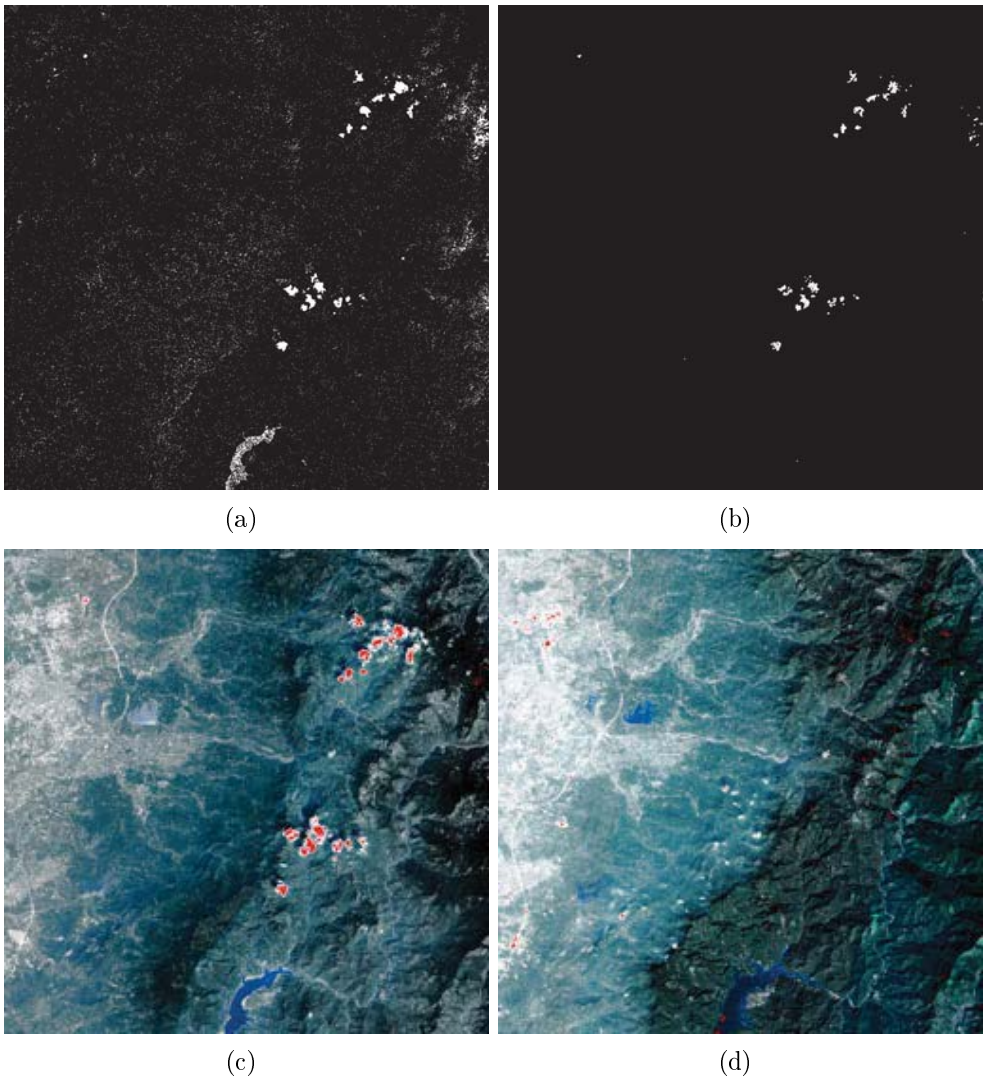

FIGURE 5. The gradient-based cloud detection. (a) The low-gradient regions. (b) Excluding low-difference area from (a) and then eliminating the small fragments. (c) Superimposing on the source image. (d) Another case of detection result.

the proposed *eHSI* color space, the intensity components of the white cloud areas are all enhanced near 1. Therefore, a fixed intensity threshold (e.g., 0.97) can be used to completely extract the white cloud areas, as shown in Figure 6(b). It is noted that the boundary of cloud areas are not eroded as in the results produced by the previous two methods; however, some high-intensity non-cloud pixels also were extracted. Accordingly, the difference checking and the morphological *opening* operation were used to release the fixed-white land covers and small regions. The complete algorithm is described as follows.

Algorithm 3.4. *Cloud detection using white color thresholding in the eHSI color spaces.*

Step 1: *Transform two original color images, I_a and I_b, from the RGB into the proposed eHSI color space.*

Step 2: *Threshold I_a and I_b into T_a and T_b, using the intensity threshold value (0.97) in the eHSI color space.*

Step 3: *Check difference using Algorithm 3.2.*

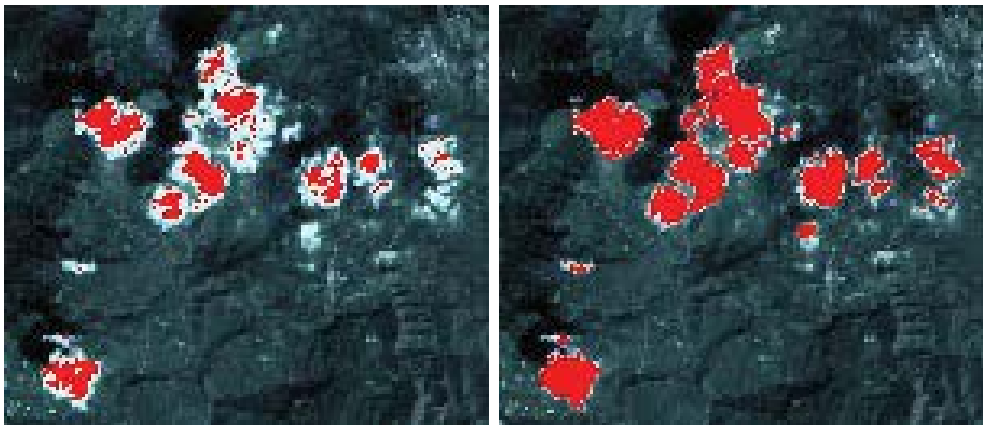

(a) (b)

FIGURE 6. The comparison of cloud extraction based on the traditional *HSI* and the proposed *eHSI* color models. (a) The cloud areas are extracted from the *HSI*-enhanced image. (b) The cloud areas are extracted from the eHSI-enhanced image. In all cases, the cloud threshold value is (0.97, 0.97, 0.97).

One example of cloud detection Algorithm 3.4 is shown in Figure 7(a) and the urban land covers were released, as shown in Figure 7(b). The final results were superimposed on the original images, as shown in Figures 7(c) and 7(d). Many broken tiny cloud areas were correctly detected, and some fixed-white land covers were successfully excluded by using the difference checking method, as depicted by the yellow circles in Figures 7(c) and 7(d).

4. **Image Mosaicking and Feathering.** The cloud and cloud-shadow regions in the base image were clipped out and replaced by the corresponding regions from the replacing images (i.e., other temporal images). The determination of replaceable regions will be described in Section 4.1. Mostly, the seams appear in the adjacent areas between the original base image and the replaced regions. Image feathering is a process to make the seam invisible. A multiscale weighting mask was created for image feathering. The feathering steps consist of color matching and pyramid multiscale feathering; these steps will be described in Sections 4.2 and 4.3, respectively.

4.1. **Determining the augmented zone.** To handle the fragmentary cloud regions that surround the detected cloud areas, the base image was segmented into 32×32-pixel zones. If the number of cloud pixels in one zone is greater than five, this zone will be labeled as the cloud zone, and it will be replaced by the same-position zone in the other temporal images. As an example, in Figure 8(a), the black zones that include the cloud pixels were labeled as the cloud zones. Furthermore, to remove the cloud shadow areas and the thin cloud areas appearing beside the detected cloud areas, the augmented zones were created to augment the cloud zones. The augmented zones were determined by the eight-neighbor grid zones around the cloud zones, as the gray zones shown in Figure 8(a). If the same-position zone in the other temporal images has more than five cloud pixels, the augmented zone will be removed, as depicted by the yellow circle in Figure 8(a).

In general, the multiple temporal images have different levels of brightness, caused by atmospheric effects, sun angles, and sensor viewing angles. After the cloud and augmented zones were replaced by the same-position zones in other temporal images, the seams

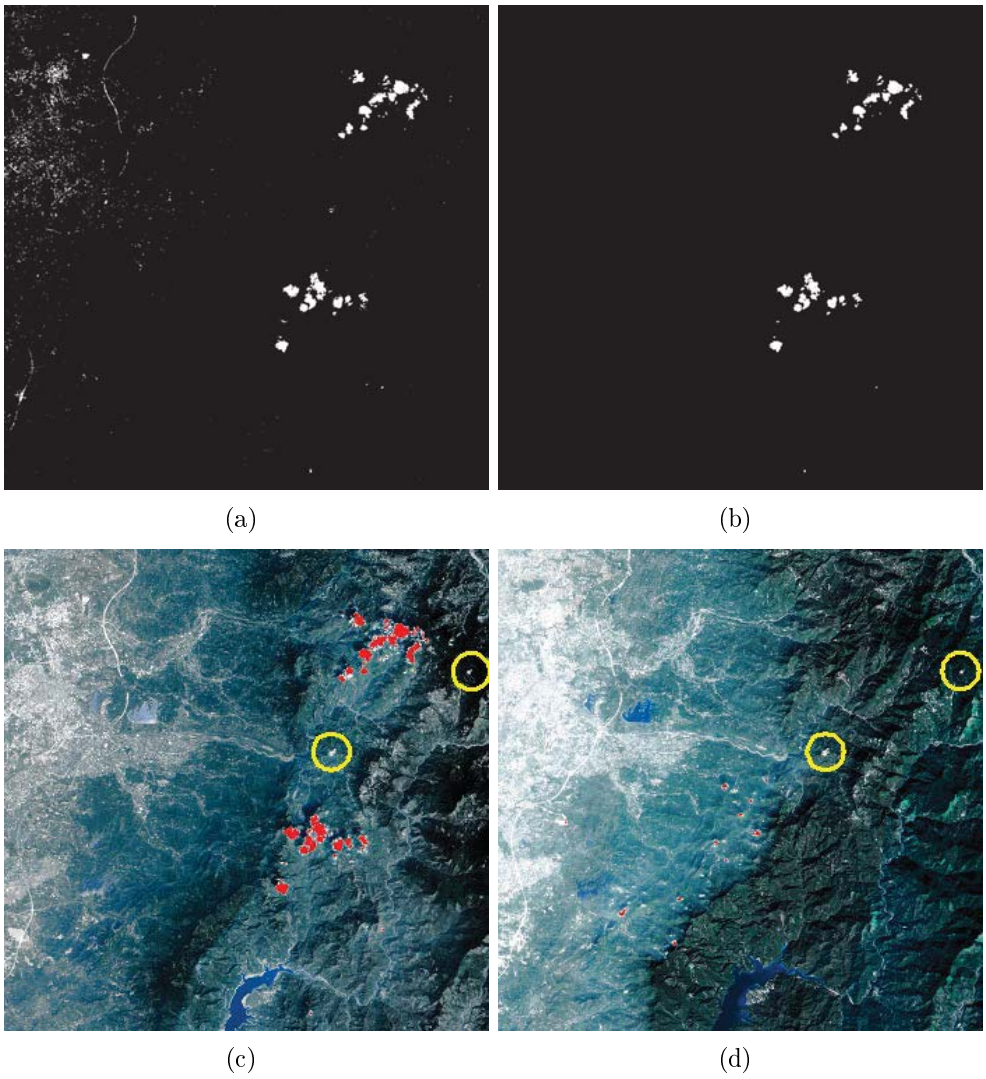

(a) (b)

(c) (d)

FIGURE 7. The intensity thresholding-based cloud detection. (a) The high intensity areas. (b) Eliminating the low difference areas from (a) and then eliminating the small fragments. (c) Superimposing on the source image. (d) Another case.

appeared in the adjacent areas between the base image and the replaced regions, as shown in Figure 8(b). Therefore, a feathering procedure was required to improve the visual quality of the final results.

4.2. **Color uniformity.** Before the feathering process, a color uniformity method [27, 28] was used to make the color of the replacing image uniform with the color of the base image, based on the $l\alpha\beta$ color model; the complete algorithm is described as follows.

Algorithm 4.1. *Color uniformity between the base and the replacing images.*

Step 1: *Transform base image I_b and replacing image I_r from RGB to $l\alpha\beta$ color space.*

Step 2: *Compute the means of l, α, and β components (denoted as $\overline{l_b}$, $\overline{\alpha_b}$, and $\overline{\beta_b}$, respectively) and the standard deviations (denoted as σ_b^l, σ_b^α, and σ_b^β, respectively) of the base image and the replacing image (denoted as $\overline{l_r}$, $\overline{\alpha_r}$, $\overline{\beta_r}$, σ_r^l, σ_r^α, and σ_r^β), respectively.*

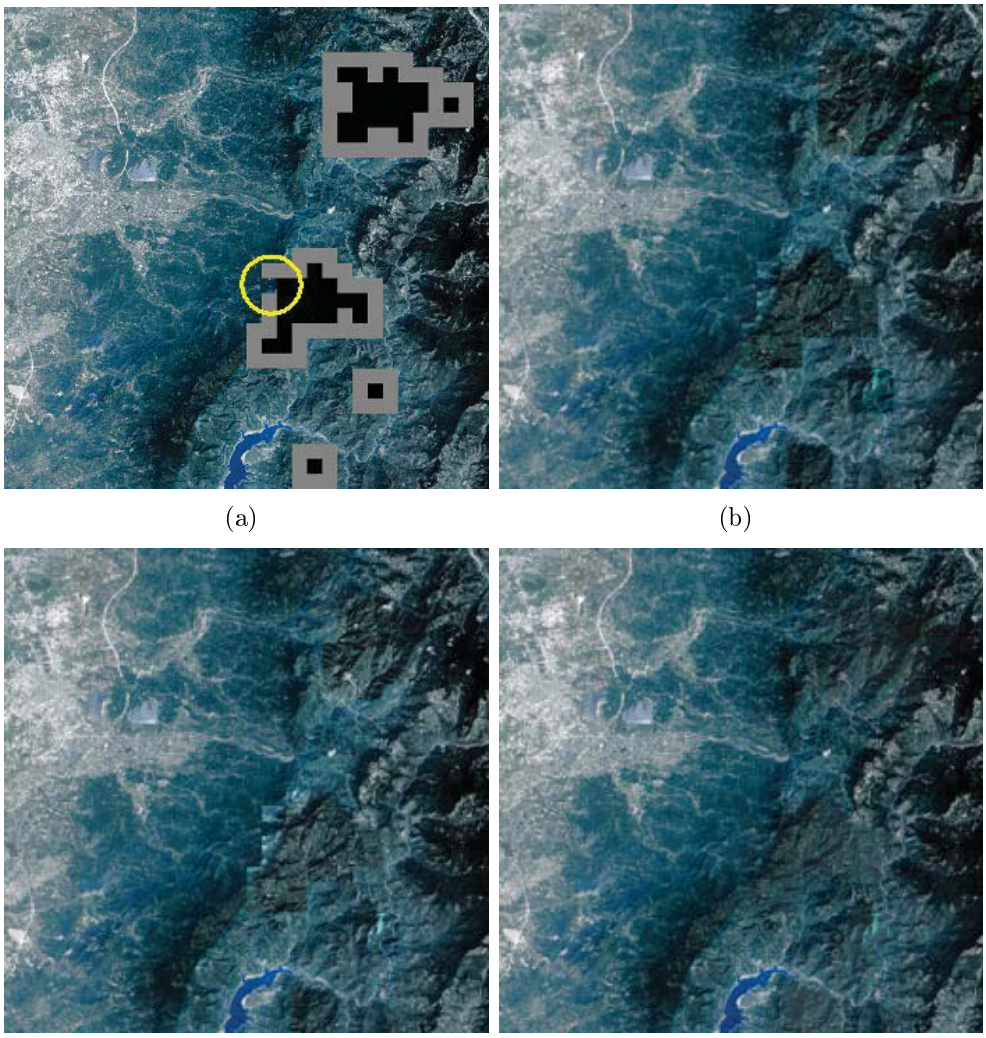

(a) (b)

(c) (d)

FIGURE 8. The cloud and the augmented zones. (a) The cloud and augmented zones are clipped from the base image. (b) The clipped zones are patched with the same zones of a non-unified replacing image. (c) The clipped zones are replaced by the same zones of the color-unified replacing image. (d) The multi-scale fusion result.

Step 3: *Substitute the l, α, and β components of the pixels in the replacing zones with, respectively, by using*

$$\begin{cases} l'_r = \dfrac{(l_r - \overline{l_r})\sigma_b^l}{\sigma_b^l} + \overline{l_b} \\ \alpha'_r = \dfrac{(\alpha_r - \overline{\alpha_r})\sigma_b^\alpha}{\sigma_r^\alpha} + \overline{\alpha_b} \\ \beta'_r = \dfrac{(\beta_r - \overline{\beta_r})\sigma_b^\beta}{\sigma_r^\beta} + \overline{\beta_b} \end{cases} \tag{19}$$

Step 4: *Transform the pixels in the replaced zones from $l\alpha\beta$ color space back to RGB color space.*

The uniformity process made the color of the replacing zones more similar to the base image, as shown in Figure 8(c). However, the color differences between the adjacent sides

of the seams are still visible, and they will be further processed by the following feathering process.

4.3. **Multi-scale feathering.** The multiscale pyramid method [15] has been used in many applications that include stitching and feathering two different images. The method will be used to remove the seam between the replaced zones and the base image; the complete algorithm is described as follows.

Algorithm 4.2. *Pyramid multi-scale feathering algorithm.*

Step 1: *Decompose the base and the replacing images into m different resolution images to create the Gaussian pyramids, denoted as* $G_1, \ldots, G_m$, *respectively.*

Step 2: *Separately obtain the Laplacian pyramids of the base and replacing images from the difference between every two contiguous resolution images:*

$$L_l = G_l - EXPAND[G_{l+1}] \tag{20}$$

where L_l *is the* l*-th level of the Laplacian pyramid, and the EXPAND function is defined as*

$$EXPAND[G_{l+1}] = G'_l(i,j) = \frac{1}{\alpha(i,j)} \sum_{m=-2}^{2} \sum_{n=-2}^{2} G_{l+1}\left(\frac{i+m}{2}, \frac{j+n}{2}\right) \tag{21}$$

where

$$\alpha(i,j) = \begin{cases} 4, & \text{if both } i \text{ and } j \text{ are odd,} \\ 6, & \text{if one of } i \text{ and } j \text{ is odd and the other is even,} \\ 9, & \text{if both } i \text{ and } j \text{ are even.} \end{cases}$$

In Equation (21), only integer $(i+m)/2$ *or* $(j+n)/2$ *is included in the summation term.*

Step 3: *Create fusion weight masks by decomposing the detected cloud regions into m level Gaussian pyramids, denoted as* $w_1, \ldots, w_m$.

Step 4: *Fuse the corresponding levels of the Laplacian pyramids of the two images with the corresponding fusion weight mask. For each level* l *and pixel* (i,j),

$$LS_l(i,j) = w_l(i,j)LB_l(i,j) + [1 - w_l(i,j)]LR(i,j) \tag{22}$$

where LS_l, LB_l, *and* LR_l *are the* l*-th level Laplacian pyramids of the fused, base, and replacing images, respectively, and* w_l *is the* l*-th level fusion weight mask.*

Step 5: *Repeatedly construct the finer Gaussian pyramid* GS_l *from the fused* LS_l *and the coarser level* $GS_l + 1$*:*

$$GS_l = LS_l + EXPAND[GS_{l+1}] \tag{23}$$

until the fused image GS_0 *is obtained, where* $GS_N = LS_N$.

One example of the fused result is shown in Figure 8(d), where the seams between the replacing regions and the base image were feathered and disappeared.

5. **Experiments and Discussions.** The 6.25-meter-resolution synthesized *SPOT* images were used to evaluate the proposed approaches. These source images show the same regions, but they were captured in different years. Two *SPOT* images near the Tseng-Wen Reservoir captured in years 2001 and 2000 are shown in Figures 3(a) and 3(b), respectively. In this example, the 2001 image was selected as the base image. After image enhancement on the proposed *eHSI* color space, the cloud pixels were easily extracted by the simple intensity thresholding method in the *eHSI* color space, as shown in Figures 7(c) and 7(d). The cloud and augmented zones were determined as shown in Figure

8(a) and were replaced with the corresponding zones in the replacing image, as shown in Figure 8(b). Finally, the replacing zones were color-unified, as shown in Figure 8(c), and feathered by the multiscale pyramid method, as shown in Figure 8(d). Another case is shown in Figure 9, in which the source images have more differences in brightness and contrast, but the case also shows a good cloud removal result.

The purpose of this study is for applications of geographical visualization, such as Google Earth; thus, all clouds to be removed are small scale. For most cases, two different temporal images are enough to produce a satisfactory cloud-free image. However, if clouds appear in the same location in both source images, additional temporal images are required for retrieving the cloud-free pixels.

The results of cloud removal on natural aerial images are difficult to evaluate quantitatively, because the multi-temporal images vary in brightness and cloud cover. Here, only the cloud detection techniques are quantitatively compared. The procedure for cloud removal generally consists of detecting cloud pixels and then replacing them with non-cloud pixels; as such, we compared the cloud detection performances of various cloud detection methods, described in Section 3. In this comparison, the cloud pixels in the source images were manually labeled to construct the ground truth. There are a total of 4,194,304 pixels in the source images, and 13,853 pixels are labeled as cloud pixels. Four cloud detection methods: the *PWD*, gradient, *LSU*, and intensity thresholding methods, were compared; the results are shown in Table 1. The evaluation criteria included Type I error, Type II error, and the detection rate. Type I error means missed detection of cloud pixels, and is also called "false positive". Type II error means classifying the non-cloud pixels as cloud pixels, and is also called "false negative" or "false alarm". Detection rate is the ratio of correctly detected cloud pixels to all cloud pixels. The unit of Type I and II errors is the number of pixels. It is noted that difference checking is used to release fixed-flat land covers; thus, the number of false alarms encountered when using the methods with additional difference checking is obviously reduced. However, some small cloud areas may be removed by the *opening* operation; thus, the detection rate is slightly decreased.

As described in Section 3, it is difficult to detect the boundaries of cloud areas with *PWD* and the gradient methods; thus, their detection rates are low. On the other hand, the *LSU* and intensity thresholding methods are different approaches to the same purpose, and both have high detection rates. After the images were enhanced in the *eHSI* color space, the cloud pixels were more concentrated in the high-intensity range, so the proposed intensity thresholding method is more accurate. Furthermore, the computation complexity of intensity thresholding is lower than with the *LSU* method. Although the *LSU* method has a better detection rate than that of the intensity thresholding method, it also has more false alarms and may result in more unnecessary additive processes. The proposed "intensity thresholding + difference checking" approach produces the least Type I + Type II errors.

6. **Conclusions.** In this research study, a multidisciplinary approach was proposed to synthesize high-quality, cloud-free images from multi-temporal aerial images. The proposed approach has the following characteristics: (*i*) an intensity histogram equalization in the proposed *eHSI* color space was used to enhance the intensity and saturation components of the original images; (*ii*) the intensity thresholding in the *eHSI* color space, accompanied by difference checking, was proposed for cloud pixel determination; (*iii*) a contour band composed of augmented zones for the cloud zones was designed for image mosaicking; (*iv*) $l\alpha\beta$ color matching was used to unify the color of the base and replacing images; (*v*) a pyramid multiscale fusion method was used to feather the resulting image, making the seams invisible. We placed a great deal of effort into the color processing

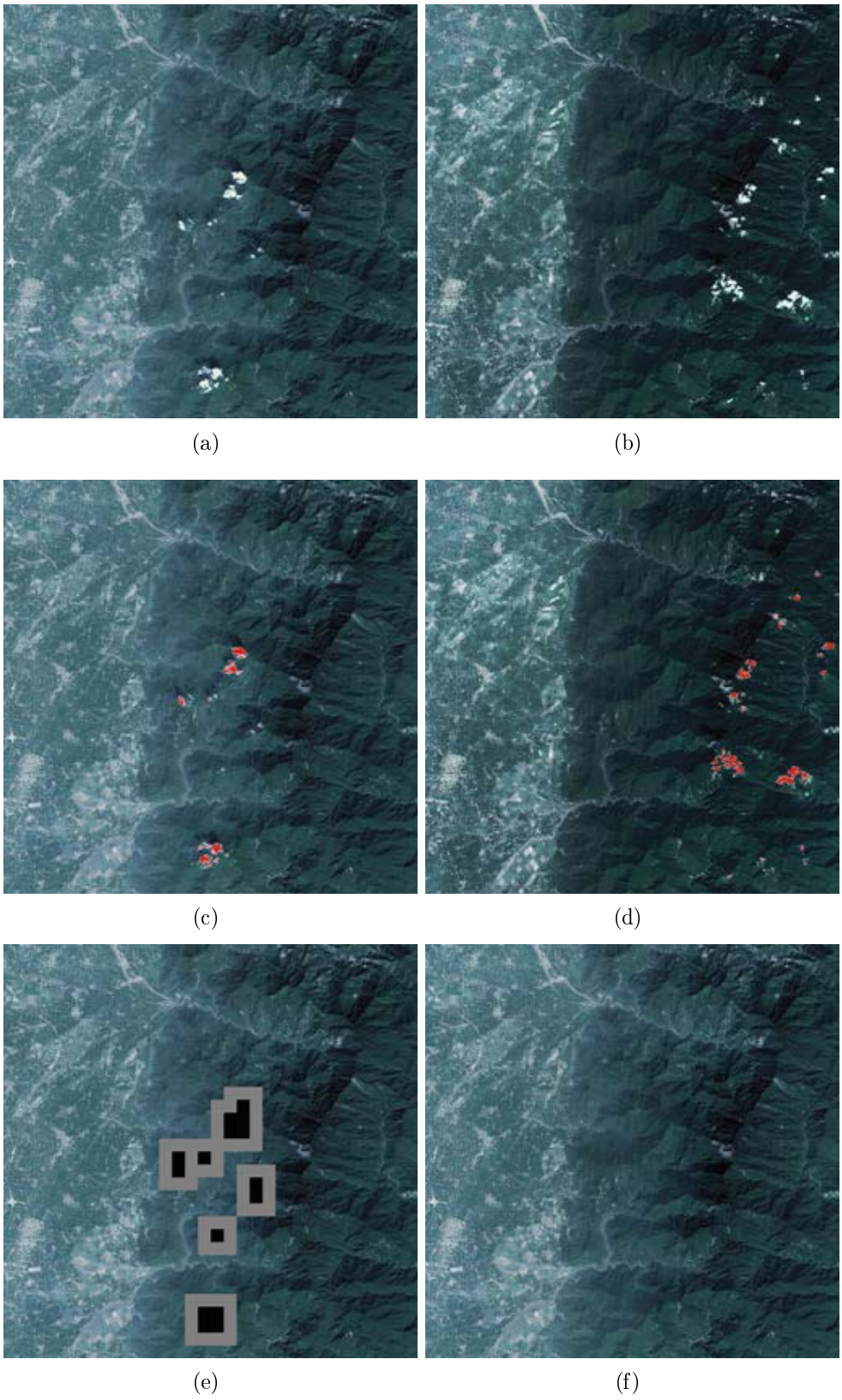

FIGURE 9. Another example of cloud removal. (a) and (b) The original cloud images. (c) and (d) The detected cloud regions by using the eHSI-based intensity thresholding with difference checking method. (e) The cloud and augmented zones. (f) The final fusion result.

TABLE 1. The comparison of cloud detection among the eight methods

Methods	Type I error	Type II error	Detection rate
PWD	6,461	136,419	53.36%
PWD + Difference Checking	9,222	5,008	33.43%
Gradient	7,539	514,329	45.58%
Gradient + Difference Checking	9,646	4,207	30.37%
LSU	136	108,321	99.02%
LSU + Difference Checking	2,261	39,409	83.68%
Intensity Thresholding	354	61,294	97.44%
Intensity Thresholding + Difference Checking	925	1,425	93.33%

in order to synthesize high-quality images with proper brightness and saturation. The results fit human visual perception quite well, and they achieve practical applications.

The procedure steps of this study: image enhancement, cloud detection, image mosaicking, and image feathering, are partially the same as in our previous work [26]; however, they were all improved in effect and efficiency. First, the source images were enhanced in the *eHSI* color space, so that the gamut problem never occurred. Second, the cloud areas were detected by the intensity thresholding method in the *eHSI* color space, so that not only was accuracy increased, but also, computation complexity was reduced. Finally, the proposed fusion weight mask was used to feather the replacing regions and the base image, so that the feathering was isotropic, and computation complexity was reduced.

REFERENCES

[1] C. Feng, J. Ma, Q. Dai and X. Chen, An improved method for cloud removal in ASTER data change detection, *Proc. of Int. Geoscience and Remote Sensing Symp.*, Anchorage, Alaska, pp.3387-3389, 2004.

[2] P. Arellano, *Missing Information in Remote Sensing: Wavelet Approach to Detect and Remove Clouds and Their Shadows*, Master Thesis, Int. Institute of Geo-information Science and Earth Observation, Enschede, The Netherlands, 2003.

[3] B. Wang, A. Ono, K. Muramatsu and N. Fujiwara, Automated detection and removal of clouds and their shadows from Landsat TM images, *IEICE Trans. on Information and Systems*, vol.82, no.2, pp.453-460, 1999.

[4] M. Kubo, H. Koshinaka and K. I. Muramoto, Extraction of clouds from satellite imagery in the Antarctic using wavelet transform and Mahalanobis classifier, *Proc. of IEEE Int. Geoscience and Remote Sensing Symp.*, Sydney, Australia, vol.5, pp.2158-2160, 2001.

[5] Z. Li, Z. Jing, X. Yang and S. Sun, Color transfer based remote sensing image fusion using non-separable wavelet frame transform, *Pattern Recognition Letters*, vol.26, pp.2006-2014, 2005.

[6] U. Amato, A. Antoniadis, V. Cuomo, L. Cutillo, M. Franzese, L. Murino and C. Serio, Statistical cloud detection from SEVIRI multispectral images, *Remote Sensing of Environment*, vol.112, pp.750-766, 2008.

[7] Y. S. Choi, C. H. Ho, M. H. Ahn and Y. M. Kim, An exploratory study of cloud remote sensing capabilities of the communication, ocean and meteorological satellite (COMS) imagery, *Int. Journal of Remote Sensing*, vol.28, pp.4715-4732, 2007.

[8] Z. Wang, J. Jin, J. Liang, K. Yan and Q. Peng, A new cloud removal algorithm for multi-spectral images, *Proc. of MIPPR 2005: SAR and Multispectral Image Processing*, Wuhan, China, pp.60430W.1-60430W.11, 2005.

[9] S. Gabarda and G. Cristóbal, Cloud covering denoising through image fusion, *Image and Vision Computing*, vol.25, pp.523-530, 2007.

[10] E. H. Helmer and B. Ruefenacht, Cloud-free satellite image mosaics with regression trees and histogram matching, *Photogrammetric Engineering and Remote Sensing*, vol.71, pp.1079-1089, 2005.

[11] M. Li, S. C. Liew and L. K. Kwoh, Generating "cloud free" and "cloud-shadow free" mosaic for SPOT panchromatic images, *Proc. of IEEE Int. Geoscience and Remote Sensing Symp.*, Toronto, Canada, vol.4, pp.2480-2482, 2002.
[12] M. Li, S. C. Liew and L. K. Kwoh, Producing cloud free and cloud-shadow free mosaic from cloudy IKONOS images, *Proc. of IEEE Int. Geoscience and Remote Sensing Symp.*, Toulouse, France, vol.6, pp.3946-3948, 2003.
[13] S. C. Liew, M. Li, L. K. Kwoh, P. Chen and H. Lim, "Cloud-free" multi-scene mosaics of SPOT images, *Proc. of IEEE Int. Geoscience and Remote Sensing Symp.*, Seattle, WA, USA, vol.2, pp.1083-1085, 1998.
[14] C.-L. Chien and D.-C. Tseng, Color image enhancement with exact HSI (eHSI) color model, *International Journal of Innovative Computing, Information and Control*, vol.7, no.12, pp.6691-6710, 2011.
[15] P. Burt and E. Adelson, The Laplacian pyramid as a compact image code, *IEEE Trans. on Communications*, vol.31, pp.532-540, 1983.
[16] T. Tateyama, Z. Nakao, X. Han and Y.-W. Chen, Contrast enhancement of MR brain images by canonical correlations based kernel independent component analysis, *International Journal of Innovative Computing, Information and Control*, vol.5, no.7, pp.1857-1866, 2009.
[17] M. F. Hossain and M. R. Alsharif, Minimum mean brightness error dynamic histogram equalization for brightness preserving image contrast enhancement, *International Journal of Innovative Computing, Information and Control*, vol.5, no.10(A), pp.3263-3274, 2009.
[18] J. Pan, C. Zhang and Q. Guo, Image enhancement based on the Shearlet transform, *ICIC Express Letters*, vol.3, no.3(B), pp.621-626, 2009.
[19] Y. Zhang, C. Zhang, J. Chi and R. Zhang, An algorithm for enlarged image enhancement, *ICIC Express Letters*, vol.3, no.3(B), pp.669-674, 2009.
[20] A. R. Weeks, G. E. Hague and H. R. Myler, Histogram equalization of 24-bit color images in the color difference (C-Y) color space, *Journal of Electronic Imaging*, vol.4, pp.15-22, 1995.
[21] R. C. Gonzalez and R. E. Woods, *Digital Image Processing*, 3rd Edition, Prentice Hall, Upper Saddle River, NJ, 2007.
[22] L. Cohen, Time-frequency distributions-a review, *Proc. of the IEEE*, vol.77, pp.941-981, 1989.
[23] I. Daubechies, The wavelet transform, time-frequency localization and signal analysis, *IEEE Trans. on Information Theory*, vol.36, pp.961-1005, 1990.
[24] K. H. Brenner, A discrete version of the Wigner distribution function, *Proc. of EURASIP: Signal Processing II: Theories and Applications*, pp.307-309, 1983.
[25] Y. H. Hu, H. B. Lee and F. L. Scarpace, Optimal linear spectral unmixing, *IEEE Trans. on Geoscience and Remote Sensing*, vol.37, pp.639-644, 1999.
[26] D.-C. Tseng, H.-T. Tseng and C.-L. Chien, Automatic cloud removal from multi-temporal SPOT images, *Applied Mathematics and Computation*, vol.205, no.2, pp.584-600, 2008.
[27] E. Reinhard, M. Adhikhmin, B. Gooch and P. Shirley, Color transfer between images, *IEEE Computer Graphics and Applications*, vol.21, pp.34-41, 2001.
[28] D. L. Ruderman, T. W. Cronin and C.-C. Chiao, Statistics of cone responses to natural images: Implications for visual coding, *J. Opt. Soc. Am. A*, vol.15, pp.2036-2045, 1998.